JAERI-M
83-171

FLUCTUATIONS OBSERVED IN NBI HEATED DOUBLET III DIVERTOR DISCHARGES

October 1983

S. KONOSHIMA, H. AIKAWA, M. AZUMI, K. HOSHINO
A. KAMEARI,[*1] M. KASAI,[*1] A. KITSUNEZAKI
T. KOBAYASHI,[*2] T. MATSUDA, N. MIYA, M. NAGAMI
H. NINOMIYA, S. SENGOKU, M. SHIMADA
T. TOKUTAKE, H. YOKOMIZO, T. YAMAUCHI
T. ANGEL,[*3] C. ARMENTROUT,[*3] F. BLAU[*3]
G. BRAMSON,[*3] N. BROOKS,[*3] E. FAIRBANKS[*3]
C. HSIEH,[*3] G. JAHNS,[*3] R. SERAYDARIAN[*3]
R. SNIDER,[*3] R. STAMBAUGH[*3] AND E. STRAIT[*3]

日 本 原 子 力 研 究 所
Japan Atomic Energy Research Institute

JAERI-M レポートは，日本原子力研究所が不定期に公刊している研究報告書です。
入手の問合わせは，日本原子力研究所技術情報部情報資料課（〒319—11 茨城県那珂郡東海村）あて，お申しこしください。なお，このほかに財団法人原子力弘済会資料センター（〒319-11 茨城県那珂郡東海村日本原子力研究所内）で複写による実費頒布をおこなっております。

JAERI-M reports are issued irregularly.
Inquiries about availability of the reports should be addressed to Information Section, Division of Technical Information, Japan Atomic Energy Research Institute, Tokai-mura, Naka-gun, Ibaraki-ken 319-11, Japan.

編集兼発行　日本原子力研究所
印　　刷　山田軽印刷所

JAERI-M 83-171

FLUCTUATIONS OBSERVED IN NBI HEATED DOUBLET III DIVERTOR DISCHARGES

Shigeru KONOSHIMA, Hiroshi AIKAWA, Masafumi AZUMI, Katsumichi HOSHINO
Akihisa KAMEARI[*1], Masao KASAI[*1], Akio KITSUNEZAKI, Tomofumi KOBAYASHI[*2]
Toshiaki MATSUDA, Naoyuki MIYA, Masayuki NAGAMI, Hiromasa NINOMIYA
Seio SENGOKU, Michiya SHIMADA, Toshikuni TOKUTAKE, Hideaki YOKOMIZO
Toshihiko YAMAUCHI, T. ANGEL[*3], C. ARMENTROUT[*3], F. BLAU[*3], G. BRAMSON[*3]
N. BROOKS[*3], E. FAIRBANKS[*3], C. HSIEH[*3], G. JAHNS[*3], R. SERAYDARIAN[*3]
R. SNIDER[*3], R. STAMBAUGH[*3] and E. STRAIT[*3]

Department of Large Tokamak Development, Tokai Research Establishment, JAERI
(Received September 30, 1983)

A specific type of activity associated with fairly large pulsive energy loss has been observed, predominantly during improved confinement (H-mode) discharges in the NBI heated Doublet III tokamak. Large repetitive bursts of edge recycling light with 2-5ms duration and ~10ms intervals appear in the course of increasing β_p. The amount of energy released by a single burst is estimated to be at least 2-3% of stored energy. As a result of these periodic energy losses, attained values of plasma energy is evaluated to be depressed as much as 10%. Prior to a burst, large m=n=0 magnetic field oscillations of ~20kHz were observed with highly peaked distribution near the divertor region. No other particular activities which might be responsible for either the confinement deterioration or improvement have been found throughout the entire operational space.

Keywords: Fluctuations, NBI Heated, Doublet III, Divertor Discharges, Energy Loss, H-mode, Plasma Confinement, Tokamak Bursts

---

This work was performed under a cooperative agreement betwen the Japan Atomic Energy Research Institute and the United States Department of Energy under DOE Contract No. DE-AT03-80SF11512.

*1 Mitsubishi Atomic Power Industries., Inc.
*2 Hitachi, Ltd.
*3 GA Technologies, Inc., U.S.A.

中性粒子入射加熱されたダブレットⅢのダイバータ放電時に観測される揺動

日本原子力研究所東海研究所大型トカマク開発部
木島　滋・相川　裕史・安積　正史・星野　克道
亀有　昭久[*1]・笠井　雅夫[*1]・狐崎　晶雄・小林　朋文[*2]
松田　俊明・宮　直之・永見　正幸・二宮　博正
仙石　盛夫・嶋田　道也・徳竹　利国・横溝　英明
山内　俊彦・T. ANGEL[*3]・C. ARMENTROUT[*3]
F. BLAU[*3]・G. BRAMSON[*3]・N. BROOKS[*3]
E. FAIRBANKS[*3]・C. HSIEH[*3]・G. JAHNS[*3]
R. SERAYDARIAN[*3]・R. SNIDER[*3]
R. STAMBAUGH[*3]・E. STRAIT[*3]

（1983年9月30日受理）

かなり大きな間歇的エネルギー損失を伴う独特のアクティビティーが，中性粒子入射加熱時のダブレットⅢトカマクにおいて，しかも専ら閉じ込めの良い（Hモード）放電時に観測された。ポロイダルベータ値が上昇していくと，パルス幅2−5msecで約10msecの間隔をもつ周辺リサイクリング光の大きなバーストの繰り返しが見られる。1回のバーストによってはき出されるエネルギー量は蓄積全エネルギーの少なくとも2−3％に相当すると見積られる。この周期的エネルギー損失は，プラズマエネルギーの最大到達値にして10％程抑制されている事に相当する。バーストに先立って，ダイバーター部に大きなピークをも約20KHzでm＝n＝0の大きな磁場の揺動が観測された。これ以外に，全運転領域を通じて一般的に閉じ込めの劣下或いは改善を支配していると思われるような特別のアクティビティーは観測されていない。

＊1　外来研究員；三菱原子力工業㈱
＊2　外来研究員；日立製作所㈱
＊3　GAテクノロジーズ

Contents

目　　次

1. Introduction

MHD activity in tokamak plasmas has been extensively studied in theories and experiments. However, there is quite a bit of information of particular activities which could definitely determine plasma properties; such as internal disruption and some cases of hard disruption. In many of the cases, it is obscure whether the activity itself plays an essential role in particle and/or energy transport or is just a simple indication of local profile changes. In this context, it is important to evaluate the influences introduced by each activity.

Experiments on high power neutral beam injection (NBI) heating demonstrated that the high beta plasmas close to a reactor relevant level are well sustainable, even in a situation where confinement is degraded to some extent [1]. Several attempts have been made to clarify the cause of the degradation from the viewpoint of MHD activity in higher β. In ISX-B, the existence of high frequency broad band spectrums on the Mirnov signal is thought to be an indication of the resistive ballooning mode and the enhanced thermal diffusivity due to this activity is estimated [2]. A particular type of $m=1$ activity called "fish bone" is reported as one of the important loss mechanisms for high energy ions in PDX [3]. However, in Doublet III we were not able to find any evidence of activities which indicate positive correlations with observed deterioration or empirical scaling which is reported in [1] although the measurement was restricted to one internal magnetic probe with 25μsec time resolution. Also, there was no marked MHD activity which affected the basic heating efficiency in JFT-2 [4].

Recently, discharges with improved confinement time comparable to the ohmic level (H-mode) have also been obtained in Doublet III, similar to the ones already reported in ASDEX [5]. The H-mode discharge is characterized by gradual growth of plasma energy indicated by a diamagnetic signal after abrupt reduction of edge recycling neutral light (D_α/H_α), contrast to limiter discharges in which the energy saturates within 50-100ms and accompany enhanced neutral light emission. Detailed values of plasma parameters and characterisitcs are to be reported [6]. Fluctuations in H-mode discharges are characterized as follows: large amplitude m=3,4 Mirnov oscillations coupled with internal m=1 mode; longer repetition sawtooth with faint amplitude; and, in addition, the appearance of large, almost regular bursts of recycling light. This paper describes the characteristics of D_α/H_α burst activity (which may rather be called edge relaxation oscillation phenomena) in detail. Similar observations were also reported in ASDEX [7], although there is a major difference in density modulation.

2. Diagnostics

Description of the Doublet III tokamak, neutral beam injectors are found elsewhere [1,8]. Major machine parameters are $B_T \lesssim 2.4T$, $I_p \lesssim 1MA$, $R \simeq 143cm$ and $a \simeq 43cm$. Neutral hydrogen beams of ~70kV are injected into deuterium plasma nearly perpendicularly. Maximum available NBI power was ~4.5MW. The diagnostics mainly used in the fluctuation study are the following:

1) Poloidal magneic field fluctuation (Mirnov oscillation) ; $\tilde{B}_\theta$

Figure 1(a) shows the locations of 11 magnetic probes in the poloidal direction $(300° (\equiv -60°)) \leq \theta \leq 240°$ with every 30° separation at the toroidal angle $\psi = 255°$). Another $\tilde{B}_\theta$ probe is located at $\theta = 0°$ and $\psi = 75°$ (180° apart) for the identification of toroidal mode structure. Probes are attached inside the vacuum vessel wall and behind the limiters with ~0.6mm stainless steel covers. The sensitivity of each probe is calibrated (in the absence of the vessel wall) and have nearly flat frequency response of ~0.15 [turn-m^2] up to ~20kHz. Actual time resolution of $\tilde{B}_\theta$ is restricted by a digitizer clock rate of 10μsec minimum.

2) Soft x-ray diodes (PIN diode) arrays ; $\tilde{A}$

Soft x-ray emission profile from main plasma (photon energy with ≥1.1-1.3keV) can be measured by two fan-shaped arrays (vertical and tangential arrays with 3-4cm spatial resolution). The regions yielding maximum emissivity are shown by arrows in Fig. 1(a) (i.e., +36cm ≥ z(vertical) ≥ -24cm and +21cm≥R (radial : R_o=143cm) ≥ -5cm). The signal is divided with a high pass (SXRF : $1.3kH_z \leq f \leq 50kHz$) and low pass (SXRS : $f \leq 1.3kHz$) filters.

3) Multichannel grating cyclotron radiometer ; $2\Omega_{ce}$

Time and spatial resolutions are 5kHz (digitizer) and ~7cm vertically and ~3cm horizontally. The spatially covered zone is $-11\text{cm} < R_o < 27\text{cm}$ for B_T ~2.3T. The absolute value of the intensity could be calibrated by Thomson scattering via Michelson $2\Omega_{ce}$ radiometer.

4) D_α/H_α emission by filtered photo diodes ; HALPHA

Three filtered photo diodes (λ_o=6563Å with $\Delta\lambda$(FWHM) ~ 100Å) looking at the primary limiter surface (HALPHALİM), main plasma (apart from the limiters) (HALPHAU) and near the divertor region (HALPHAM) are employed with time resolution of ~0.5msec. In this paper, these recycling lights are referred to as "D_α/H_α" or "HALPHA", although the major component of the signal is D_α (main plasma) including a small fraction of H_α (from NBI).

5) Perpendicular charge exchange flux (c.x.) measurement

Injected beam and slowing down components of H atoms and bulk thermal D atoms are detected with ~130 energy channels. The orientation is set to be at the same angle as that of the NBI. Minimum time resolution is 1msec.

6) Twenty-one channel bolometer array for c.x. and radiation [9]

Response time of the bolometer is ~1msec and the radiation intensity is calibrated when $\tilde{B}$ is small enough.

7) Diamagnetic measurements

The values of the poloidal beta (β_p), toroidal beta (β_T) and stored energy (w), in which beam components are included, are obtained from diamagnetic measurements in this paper. Signals obtained from the diamagnetic loop, which is coupled with the orientation compensating coils, are numerically subtracted from the influences of the various field coil currents and vessel current [10].

The agreement between β_p measured by diagmanetism and the one calculated from density and temperature measurment is within ± 0.15 or better at low to medium plasma current; the diamagnetic value gives ~ 0.1 higher value at high I_p ($I_p \sim 700$kA) in these H-mode divertor discharges. The argument is ambiguous to some extent, since the information about the actual pressure anisotropy is not available.

3. Characteristics of H-mode Discharges and their MHD Activities

The best heating efficiency has been obtained with the equilibrium configurations shown in Figs. 1(a) and (b). Major modifications from those previously reported [11] are the extension of the main plasma downward and the ability of the scrape-off plasma to flow into both the inside and outside of the vessel wall. The minimum distance between the main separatrix magnetic surface and the limiters is estimated to be typically 3-5cm from the equilibrium calculation (in some cases of high I_p, the plasma shifts to the inside more closely).

The quantitative criteria between the H and L mode has not yet been clarified. The reason mainly comes from the fact that the values of the heating efficiency scattered continuously from the best discharges (typical H-mode) to the worst case (almost the same as the previous limiter discharges [1]) (cf. Fig. 6). However, as one of the most probable causes, the differences in the level of the edge recycling light emission is discussed in a separate paper [6]. In general, good H-mode discharges require a reduced gas puffing rate during NBI, higher I_p and higher beam power.

Several common features are observed in the H-mode discharges in contrast to the typical limiter discharges (or L-mode). Confinement improvement is clearly seen in the smooth increase of the stored plasma energy by diamagnetic signal and increase of the soft x-ray and neutron emissions without marked saturation at the early phase (50-100ms) of the NBI. With a few exceptions in low I_p, good H-mode discharges usually accompany large amplitude $m=3,4$ oscillations coupled with internal $m=1$ mode, sawtooth activity with longer repetition time which is roughly proportional to the β_p increase and D_α/H_α bursts in the course of stored energy increase.

Figure 2 shows the parameter (β_T-β_p) space which has been obtained in these experiments. Maximum values of β_T and β_p achieved are 2.4% and 1.7, respectively. All the data points are 4 beam injection (P_{INJ} ~4.5MW) case and are selected to indicate typical extremes in this space. The safety factor q_a* is simply defined for convenience to be the same as the limiter discharges, $q_a^* = (B_T/\mu_o I_p)\ (2\pi a^2/R)\ (1+K_a^2)/2$, even though the divertor configuration is employed.

The Mirnov oscillation of these discharges are characterized as the poloidal mode number of m=3 or 4, toroidal mode number of n=1 and the frequency range from several to 20kHz, excpet for the region marked "e" (low I_p case). The level of the relative amplitude $\tilde{B}_\theta/B_\theta$ has a general trend of increasing with the β_p increase from 0.1 to several percent. Figure 3 and 7 show examples of the time evolution of the Mirnov signals. They can be classified into three different types: (1) continuously growing type (Fig. 7) and (2) repetitive bursts type (Fig. 3) of large amplitude m=3,4 oscillation until the internal disruption and (3) no regular sinusoidal oscillation with m=0, n=0 perturbation occasionally. The poloidal mode structures are identified in the outer half of the cross section ($-60° \leq \theta \leq 90°$) and diminish at the inner region, usually in the case of (1) or (2). Also, these m=3,4 oscillations are coupled with an internal m=1 mode of the soft x-ray emission in their frequency and timing. Discharges marked "a", "b" and some cases of "c" in Fig. 2 are categorized as type (1) of the above-mentioned and "d" and some of "c" belong to type (2). The group of discharges marked "e" correspond to type (3).

It has already been reported that the MHD activity during high pwoer NBI exhibits several different behaviors compared to ohmic discharges. A continuous growing mode similar to type (1) was observed in JFT-2 [12] and ISX-B [13]; the burst-like type (2) are called "fish-bone" in PDX[3], although whether these types are identical to those observed in other tokamaks or not is still unclear. The hatched region in Fig. 2 corresponds to the onset of the fish-bone activity oserved in PDX [3]. However, as shown in Fig. 3(a) there is no appreciable loss of slowing down beam particles (TRRP 61-64 H) or decrease in the neutron emission (NEUTI2) correlated with the $\tilde{B}_\theta$ bursts activity onset, although the time resolution of c.x. and neutron measurements are relatively slow and 1ms and several to 10ms, respectively. Marked time correlation is seen in dips of soft x-ray emission (SXRS20) with D_α/H_α bursts rather than $\tilde{B}_\theta$ bursts. Almost all the cases ("a", "c" and some of "b" and "e" in Fig. 2) exhibit D_α/H_α burst activity.

4. D_α/H_α Bursts and Associated Phenomena at Higher β_p H-mode Discharges

Typical examples of discharges which accompany D_α/H_α bursts are shown in Figs. 4(a) : shot No. 33704 and 4(b) : shot No. 33318. The global plasma parameters of these discharges (presented in detail in this Section) are the following: #33704 : I_p = 0.62MA, $B_T \simeq 2.3$T, β_p max $\simeq 0.9$ and stored plasma energy W $\simeq$ 230kJ; #33318 : I_p = 0.49MA, $B_T \simeq 1.8$T, β_p max $\simeq 1.2$ ($\beta_T \simeq 1.5\%$) and W $\simeq$ 180kJ. Both discharges have a similar density of $\bar{n}_e \simeq 4.5\text{-}4.7\times10^{13}$ cm^{-3}, almost identical q_a^* of $\simeq 3$ and the same injection power P_{INJ} of $\simeq$ 4.5MW.

Nearly regular D_α/H_α bursts at $\simeq$ 10ms intervals are seen in all locations. Soft x-ray emissions exhibit a large sawtooth-like drop corresponding to each burst, especially at the outer radius (SXRS20 : Z = +24cm). Figure 4(b) shows that even at the central region the emission is also modulated (SXRS25 : Z=0). Stored plasma energy (DIAMAG) is slightly saturated (at $t \gtrsim$ 880 ms in Fig. 4(a)) or even decreases (4(b)) by the onset of these activities.

Figure 5 is a plot of the relative amplitude of a D_α/H_α burst with respect to β_p for different I_p and B_T. The figure shows that the bursts appear at $\beta_p \geq 0.7\text{-}0.8$. Also, there are discharges without bursts indicated as $\Delta I/I=0$. The onset region seems to be related to I_p as indicated by curves. However, it is not simply q_a^* related if compared with lower B_T cases (open points).

Figure 6 shows a situation in which good heating discharges often accompany D_α/H_α burst activity (full circles and triangles). The increment of β_p from the ohmic level divided by the injected power is plotted as a function of I_p^{-2}, i.e., the net plasma pressure increase per unit injection power (heating efficiency). All the data points are the 3 or 4 beam injection case. Power lost by shine-through is typically $\lesssim$15% at $\bar{n}_e \gtrsim 4\times10^{13}$ cm^{-3} and data points are chosen at $\bar{n}_e > 3.5\times10^{13}$ cm^{-3}. The lower broken line corresponds to the envelope of the better limiter discharges with D shape (elongation $K_a\sim1.4$) (squares). The upper line corresponds to the best results obtained so far in the equilibrium shown in Fig. 1 (at $I_p \simeq 350$kA, $\Delta\beta_p/P_{INJ} \simeq 0.4$ has been obtained with $P_{INJ} \simeq 1.2$MW ; not shown). Roughly, a factor of two improvement is obtained if compared with the best data and limiter discharges. However, in contrast to [5], the heating efficiencies distributed from the L-mode close to the limiter discharges to the best H-mode continuously, although the same configuration (Fig. 1) was employed.

Several discharges have transition phases during NBI between the L and H modes; a particular case which showed a clear transition from the L to the H mode during NBI (like ASDEX) or the H mode discharges which turn over to the L mode by small additional gas puffing or one of the beams turning off. However, no appreciable change in the characteristics of the Mirnov oscillation were observed at these transition phases. Arrows in the figure indicate shots #33704 and #33318 which are discussed following section. Sometimes in lower q_a^* discharges, very sharp D_α/H_α bursts were observed just at the time of sawtooth relaxation. These bursts are excluded in this paper, since their origin are thought to be different (induced by heat pulses due to classical sawtooth relaxation driven by internal m=1 activity).

4.1 Modulation of Plasma Parameters Due to the Bursts

Almost all the major parameters are modulated by D_α/H_α bursts. Since many of the signals are digitized in relatively slow sampling rates (order of msec) as described in Section 2, it is basically difficult to distinguish between cause and result.

Figure 7 shows the same discharges as shown in Fig. 4 in an expanded time scale. $\tilde{B}_\theta$ signals of the inner wall ($\theta \cong 180°$) show a clear burst at the beginning of D_α/H_α bursts, while the outside $\tilde{B}_\theta$ ($\theta \cong 0°$) is unclear due to the presence of a large Mirnov oscillation of $m=3,4$ coupled with the same frequency of the internal $m=1$ mode (SXFR22). (Sawtooth activity with $m=1$ oscillation is sometimes referred to as "classical sawtooth" in this paper, although usually somewhat modified from the pure ohmic $m=1$ oscillation as described in Sec. 3). In general, D_α/H_α bursts are excited independent of the existence of the internal $m=1$ mode and associated sawtooth oscillation and Mirnov oscillation (Figs. 3 and 7).

Inward radial motions of the plasma column which correlate to the bursts are also observed as shown in Fig. 7(b). The maximum displacement in Fig. 7(b) amounts to only $\Delta R_p \lesssim 0.3$cm and is small enough to the gap between the separatrix surface and the limiters based on equilibrium calculations (Fig. 1). The vertical shift Z_p is $\lesssim 0.1$cm. These plasma motions are linked together to the change in β_p and to the change of inductance.

Figure 8 shows an example of electron temperature modulation ($\hat{T}_e$) measured by a $2\Omega_{ce}$ grating radiometer. Marked T_e dips correspond to each burst. Classical internal disruptions at t=760 ms and 840 ms with m=1 oscillations are also seen. There is a possibility of overlapping harmonics component in $2\Omega_{ce}$ measurements. The intensity could be affected only in regions of R>20cm (major radius > 163cm) by the $3\Omega_{ce}$ component in these cases.

Figures 9(a)-9(c) show the modulaion profiles of T_e and soft x-ray emission at D_α/H_α bursts and at classical sawtooth for comparison. $\hat{T}_e/T_e$ ($2\Omega_{ce}$) at bursts and at sawtooth are plotted in Fig. 9(a) for shot #33704 (Fig. 8). Figure 9(b) shows the vertical profile of the soft x-ray intensity modulation ($\hat{A}/A$) for shot #33318 indicating >100% near the edge. The comparison of the magnitude of $\hat{T}_e$ and $\hat{A}$ are shown in Fig. 9(c) for similar discharge parameters as shot #33704. The top figure is a $\hat{T}_e/T_e$ ($2\Omega_{ce}$) profile at sawtooth and precursor m=1 oscillation; the second graph shows the radial profiles of $\hat{T}_e/T_e$ and $\hat{A}/A$ at the burst; and the bottom one shows the vertical profiles of $\hat{A}/A$ at sawtooth and burst. These observations are summarized as follows: oscillation amplitude increases largely at the outer region and even the central part T_e is modulated by several percent (cf. Ref. [7]). Unlike the classical sawtooth, no inversion of the phase is observed within the region covered (arrows in Fig. 1(a)). While a large increase in divertor electron temprature at the burst is reported in ASDEX[14].

The line average density measured by tangential and vertical CO_2 interferometer arrays did not indicate any evidence of $\bar{n}_e$ modulation by bursts in excess of the inherent fluctuation level $\Delta\bar{n}_e$ of $\lesssim 0.1\times10^{13}$ cm^{-3} with 0.5ms time resolution as shown in Fig. 10. This result is different from the one observed in ASDEX in which the radial line integrated density was modulated by the bursts [7].

The amount of plasma energy released ($\hat{W}$) are estimated to be at least 2-3% of total energy per burst, based on the above measurement of the electron component. Fluctuations in the corrected diamagnetic signal indicates $\hat{W}/W$ of 1-5%, although similar fluctuation levels due to thyrister noise is also present. The overall effect on W due to the presence of bursts is evaluated as $(\tau_E/\Delta t)$ $(\tilde{W}/W)$ and typically ≈10%, here $\tau_E \simeq$ 50-60ms and repetition of the burst $\Delta t \simeq$ 10ms is taken as rough numbers. In other words, the maximum β_p (or W) could be at least 10% higher for these burst dominated discharges, if the bursts were suppressed.

Charge exchange fluxes are also affected due to the bursts. Figures 11(a) and 11(b) show the time evolution of raw neutral particle counts for different energy and species. Not only the slowing down component of the H atom (injection energy is ≃ 72±1keV in this case), but also bulk thermal components of deuterium are ejected correspond to each D_α/H_α burst. In the case of Fig. 3 there is no clear correlation with D_α/H_α bursts. Although the spatial birth position of these fast and thermal neutrals are not self-evident, increased edge neutrals and their penetration seem to be responsible for these c.x. bursts. The reason for a time delay of 3-4ms from a D_α/H_α burst to a c.x. burst as shown in Fig. 11 is not clear at present.

Figure 12 shows that the bursts are also observed in the bolometer array (line-averaged radiation and c.x. flux) signals, especially near the divertor region. Increments of the total radiation power of 0.5-1MW and 30-50% of those from the divertor region are measured, if the pickup effect due to $\tilde{B}$ is assumed to be small.

4.2 Mirnov Oscillation at Burst

There is no apparent correlation between sawtooth activity or Mirnov oscillation and the burst onset as described previously. However, whether there are any common features in detailed structures on $\hat{B}_\theta$ or not is discussed in this section.

Figure 13(a) shows an exmaple of the $\hat{B}_\theta$ signal at two bursts (t≃845ms and 860ms) for shot #33704. Marked bursts in $\hat{B}_\theta$ at the inner side ($90° \leqslant \theta \leqslant 240°$) are observed at the beginning of the D_α/H_α burst (in Fig. 3(a) also). Figure 13(b) and (c) correspond to a relatively quiescent phase (no particular mode structure is found) and a clear m=3,4 oscillation phase in expanded time scale. Neither a characteristic structure nor any phase relation is found at these initial D_α/H_α burst growing phases t≃844.7ms - 845.5ms in (b) and 859.4ms -860 ms in (c) within the 10μsec time resolution. It simply indicates the oscillation is turbulent or a higher frequency component could dominate in this phase.

Although the time resolution of the D_α/H_α signal (0.5 ms) is not small enough to identify the exact timing of the D_α/H_α burst onset, Fig. 14 shows the phases which cover the time period from just prior to the D_α/H_α rise to the beginning of the rise. The figure shows the existence of a specific one cycle m=n=0 (all in phase) oscillation with a 17-25kHz at 200-500μs intervals.

Figure 15(a) is a plot of $\tilde{B}_\theta$ amplitude of the m=0 phase with respect to the poloidal angle. Relatively large amplitude modulation is found at $\theta \simeq 120°$ and 240° which correspond to the corner of the triangular plasma shape (Fig. 1). The actual distribution of the poloidal field at each magnetic probe position in these elongated divertor shapes is shown in Fig. 15(b) which is obtained from time integrated $\tilde{B}_\theta$ signals. The characteristic pattern of B_θ is shown as follows: weak B_θ near the separatrix surface intersect to the wall and the difference between the inside ($\theta \simeq 180°$) and the outside ($\theta \simeq 0°$) becoming small at the high β_p phase. Figure 15(c) shows the $\tilde{B}_\theta/B_\theta$ profile thus obtained. The perturbation is found to be highly localized near the divertor region (θ=240°). Similar but less pronounced oscillations are already present even during the quiescent (no burst) phase, as shown in Fig. 14. Therefore, these perturbations may bring about a burst when the amplitude becomes large. A similar perturbation profile is obtained even at the m=3,4 dominant phase as shown in Fig. 16. The $\tilde{B}_\theta/B_\theta$ profile at the nearly regular sinusoidal Mirnov oscillation (circle) and distorted phase (triangle) are shown and again $\tilde{B}_\theta/B_\theta$ has a pronounced peak near the divertor by an order of 10%. The same oscillations were also observed at this time in the fast response soft x-ray signals. However, due to the weak signal-to-background ratio, the internal structure cannot be specified.

5. Discussion and Summary

No definite conclusion can be drawn about the trigger mechanism which may be responsible for the D_α/H_α burst except that m=n=0 perturbations with an order of several to 10% seem to be possible candidates as a precursor type activity. No other Mirnov activity with a growth rate slower than several tenth of a μsec and with a low m ($0<m\leq 6$) number prior to the D_α/H_α burst has been observed. Since we have almost no information on the activity of scrape-off plasmas except that an order of 100kHz oscillation was detected on the saturation current of the Langmuir probe signal at the divertor plate, the possibility of some kind of electrostatic activity in the scrape-off region cannot be ruled out.

As a result of this study the following conclusions may be made:

H-mode divertor discharges usually accompany large D_α/H_α bursts which bring a large energy loss of at least 2-3% of total energy per single burst. Prior to the burst, a specific m=n=0 oscillation which was highly perturbed near the divertor region was observed. So far, no other particular MHD activities except the D_α/H_α burst which determines the global confinement characteristics has been found.

Acknowledgement

We wish to express our appreciation to Dr. A. Colleraine and the Neutral Beam Operation group, Dr. R. Callis and the D-III Machine Operation group and other members of the Diagnostic group for their continuous effort. Special thanks are due to Dr. D. Overskei and the GA Physics group for providing their computer code to review data, to Drs. T. Hirayama, T. Takizuka, other members of the JAERI team, Drs. S. Tsuji and Y. Shimomura at JAERI for fruitful discussions, and to Dr. M. Goetz for typing the manuscript. The authors gratefully aknowledge Drs. T. Ohkawa and J. Gilleland at GA Technologies and Drs. S. Mori, Y. Iso, K. Tomabechi, Y. Obata, M. Yoshikawa, T. Iijima and N. Fujisawa for their encouragement and continued support.

References

[1] NAGAMI, M., et al., Plasma Physics and Controlled Nuclear Fusion Research (Proc. 9th Int. Conf., Baltimore, 1982) Vol. 1, IAEA, Vienna (1983) 27.
BURRELL, K., et al., Nucl. Fusion 23 (1983) 536.

[2] MURAKAMI, M., et al., ibid, 57.
CARRERAS, B. A., et al., Phys. Rev. Lett. 50 (1983) 503.

[3] JOHNSON, D., et al., ibid, 9.
McGUIRE, K., et al., Phys. Rev. Lett. 50 (1983) 891.

[4] SHIMOMURA, Y., et al., High-β Study in JFT-2, Japan Atomic Energy Research Institute Report JAERI-M 9065 (1980).

[5] WAGNER, F., et al., ibid., 43.
WAGNER, F., et al., Phys. Rev. Lett. 49 (1982) 1408.

[6] NAGAMI, M., et al., to be published in Nucl. Fusion.

[7] WAGNER, F., et al., Variation of the Particle Confinement during Neutral Injection into ASDEX Divertor Plasmas, Max-Planck-Institut fur Plasma-physik Report No. III/78, 1982.

[8] COLLERAINE, A., et al., Heating in Toroidal Plasma (Proc. 3rd Joint Varenna-Grenoble Symposium, 1982) Vol. I, Euratom (1982) 49.

[9] SHIMADA, M., et al., Nucl. Fusion 22 (1982) 643.

[10] TAYLOR, T., private communication. LUXON, J., et al., Nucl. Fusion 22 (1982).

[11] NAGAMI, M., et al., Nucl. Fusion 18 (1980) 1325.

[12] YAMAMOTO, S., et al., Nucl. Fusion 21 (1981) 993.

[13] DUNLAP, J. L.,, et al., Phys. Rev. Lett. 48 (1982) 538.

[14] SHIMOMURA, Y., et al., Nucl. Fusion 23 (1983) 869.

Figure Captions

Fig. 1 Divertor configuration (results of MHD equilibrium calculation) used in this study. Eleven internal magnetic probes are isntalled every 30° from 300° to 240°. The regions observed by tangential and vertical soft x-ray arrays are indicated by arrows. Limiters (outside primary, top backup and inside NBI armor tiles) are shown as shaded area (a). (b) corresponds to the case discussed in Section 4. The gap between the separatrix magnetic surface and the limiters is 3-5cm.

Fig. 2 Operational regime expressed in terms of β_T-β_p diagram obtained in the divertor configuration shown in Fig. 1. q_a* is simply given as $(B_T/\mu_o I_p)\ (2\pi a^2/R)\ (1+K^2{}_a)/2$. The shaded region corresponds to the threshold of the onset of fishbone activity reported in [3].

Fig. 3 Time evolution (800-880msec) of one of the H-mode discharges. Parameters are: $B_T \cong 1.8$T, $I_p = 0.49$MA, $\bar{n}_e \sim 4\times10^{13}$ cm^{-3}, $\beta_p \simeq 1.3$, $\beta_T \simeq 1.7\%$ and $P_{INJ} \simeq 4.4$MW. (a) From top to bottom: $\tilde{B}_\theta$ (θ=180°), $\hat{B}_\theta$ (θ=0° most of the $\hat{B}_\theta$ bursts are saturated due to the amplifier gain); soft x-ray fluctuation at z= -4cm (SXRF22); D_α/H_α emission near the primary limiter (HALPALIM), perpendicular c.x. flux (1ms sampling time) of slowing down beam particles with an energy range between 61-64keV (TPRP 61-64H); and thermal deuterium ions with 1-3keV (TPRP 1-3D); soft x-ray emission from the central region SXRS25) and half-way from the center(SXRS20); and neutron emission with several to 10ms time resolution (NEUTI2).

(b) One of the $\tilde{B}_\theta$ bursts in expanded time scale. 20kHz oscillations are seen both in $\tilde{B}_\theta$ (θ=0°) and soft x-ray emission (z= -4cm).

Fig. 4 Examples of H-mode discharges with typical D_α/H_α bursts. Traces are from top to bottom : D_α/H_α emission looking at the main plasma (HALPHAU), near the primary limiter (HALPHALIM) and near the divertor x-point (HALPHAM), soft x-ray emission from the central region (z=0, SXRS25) and half-way region (z = +24cm, SXRS20), diamagnetic raw signal ($\propto \frac{I_p^2}{B_T}(1-\beta_p)$; plasma pressure increases downward, DIAMAG), gas puffing rate (GASPFA) and number of injected neutral beams (BEAMPOWER), respectively. All signals in arbitrary units. The SXRS25 signal is saturated at t≈890-960ms in (a). Discharge parameters for (a) #33704 : I_p = 0.62MA, $B_T \simeq$ 2.3T, $\bar{n}_e \simeq 4.7\times10^{13}$ cm^{-3} and $P_{INJ} \simeq$ 4.5MW; and (b) #33318 : I_p = 0.49MA, $B_T \simeq$ 1.8T, $\bar{n}_e \simeq 4.5\times10^{13}$ cm^{-3}, $P_{INJ} \simeq$ 4.4MW.

Fig. 5 Onset region of D_α/H_α bursts in terms of relative intensity $\Delta I/I$ of D_α/H_α (HAPHAU) burst vs. β_p for different I_p and B_T. Line-connected points indicate the presence of bursts during those β_p changes.

Fig. 6 Increment of β_p per unit injection power ($\Delta\beta_p/P_{INJ}$) with respect to I_p^{-2}. Full and open symbols correspond to discharges with and without D_α/H_α bursts, respectively. P_{INJ} = 3.2-4.5MW. Circles and triangles are discharges at $B_T \simeq$ 2.3T-2.4T and 1.8T with divertor configuration shown in Fig. 1. Square points are obtained in simple D shape ($k_a \sim 1.4$) plasma at $B_T \simeq$ 2.4-2.3T. Arrows are the shots described in Sec. 4.

Fig. 7 Expanded signals of the discharges shown in Fig. 4 (800ms-880ms). From top to bottom: D_α/H_α emission near the primary limiter; $\tilde{B}_\theta$ signal at θ = 180°, $\tilde{B}_\theta$ at θ = 0°; high frequency component of soft x-ray signal at z = -4cm (SXRF22); soft x-ray emission at z = 24cm; radial position indicator (inward shift corresponds to downward, RPA); vertical position indicator (upper direction upward, ZP); and hard x-ray monitor without lead attenuation (HXR-UP-2), respectively, in arbitrary units. (a) : shot #33704, and (b) : shot #33318. The signal is saturated at t > 820ms in $\tilde{B}_\theta$ at θ = 0° in (b) and part of $\tilde{B}_\theta$ and SXRF22 in (a).

Fig. 8 Fluctuations in T_e evolution measured by multi-channel $2\Omega ce$ grating radiometer. Corresponding to classical sawtooth activity(SXRS25 signal is saturated at t>890ms) and the D_α/H_α bursts (shown in the top figure), Te modulation is clearly seen. m = 1 oscillation was also detected. Data is shown for R = 6.3cm, and -11cm in arbitrary units. Shot #33704 (750ms -950ms).

Fig. 9 Modulation profiles of electron temperature and soft x-ray emission at $D_\alpha/H\alpha$ bursts and classical sawtooth relaxation, including phase relations (upward is taken to be a decrease of T_e and A). (a) shows the radial profile of $\tilde{T}_e/T_e$ measured by $2\Omega ce$. Circles and squares correspond to sawtooth and $D_\alpha/H\alpha$ bursts respetively, for Shot #33704. (b) shows a vertical profile of the soft x-ray modulation $(\tilde{A}/A)$ at the burst. (c), from the top figure radial profile of $\tilde{T}_e/T_e$ $(2\Omega ce)$ at the sawtooth with m = 1 oscillation, radial profile of $\tilde{A}/A$ and $\tilde{T}_e/T_e$ at the burst and a vertical profile of $\tilde{A}/A$ for a discharge similar to shot #33704.

Fig. 10 Line-averaged electron density measured with CO_2 laser interferometers at 800-880ms, showing $\tilde{n}$. From the top: vertical line integral (CO2V) and tangential line integral with torus tangency radius R_o=102cm (CO2A), R_o=167cm (CO2B) and R_o=179cm (CO2D). In arbitrary units.

Fig. 11 Modulation of a nearly perpendicular c.x. flux (raw counts) due to the bursts. From the second figure, the slowing down component of a beam ion with energy of ~48keV, ~62keV and ~64keV, and thermal deuterium ions with ~1.6keV and ~2.6keV are shown for shot #33704 (a) and #33318 (b). The sampling time of c.x. is 1 ms.

Fig. 12 The time evolution of the bolomeer array signals during the four bursts (t = 820ms -870ms). The 5 left channels looking at the divertor region and ch. 5 -ch. 19 correspond to the main plasma.

Fig. 13 Mirnov oscillation at two particular bursts at t ≃ 845ms and 860ms for shot #33704. Figure shows from top to bottom: $\tilde{B}_\theta$ at θ = -60°, -30°, 0°, 30°, 60°, 90°, 120°, 150°, 180°, 210° and 240° (see Fig. 1(a)). The expanded time scales for the quiescent phase in the 6 ms full scale (840-846ms) (b) and the large Mirnov oscillation phase in 3 ms full scale (858-861ms)(c).

Fig. 14 $\tilde{B}_\theta$ signals including θ = 0°, ψ = 75° (top figure) exhibit one cycle m=n=0 oscillations at t = 843.6 - 844.6 ms of Fig. 13(b) prior to the $\tilde{B}_\theta$ burst at t ≃ 844.7 ms. The sampling time is 10 μs.

Fig. 15 (a) Poloidal $\tilde{B}_\theta$ amplitude distribution of m=n=0 oscillation at 844.4ms of Fig. 14. $\dot{\tilde{B}}_\theta$ (Tesla/sec) and $\tilde{B}_\theta$ (Tesla) are used in the same symbol as $\tilde{B}_\theta$ in this paper. (b) Time-averaged B_θ field distribution at ohmic (650ms) and NBI (850ms) phases. (c) $\tilde{B}_\theta/B_\theta$ distribution. Angle θ is defined in Fig. 1(a).

Fig. 16 A similar plot to Fig. 15(c) during the large Mirnov oscillation excited phase (Fig. 13(c)). Regular sinusoidal oscillation phase (circles) is shown as a comparison with the distorted phase (triangles 859.4-859.5ms).

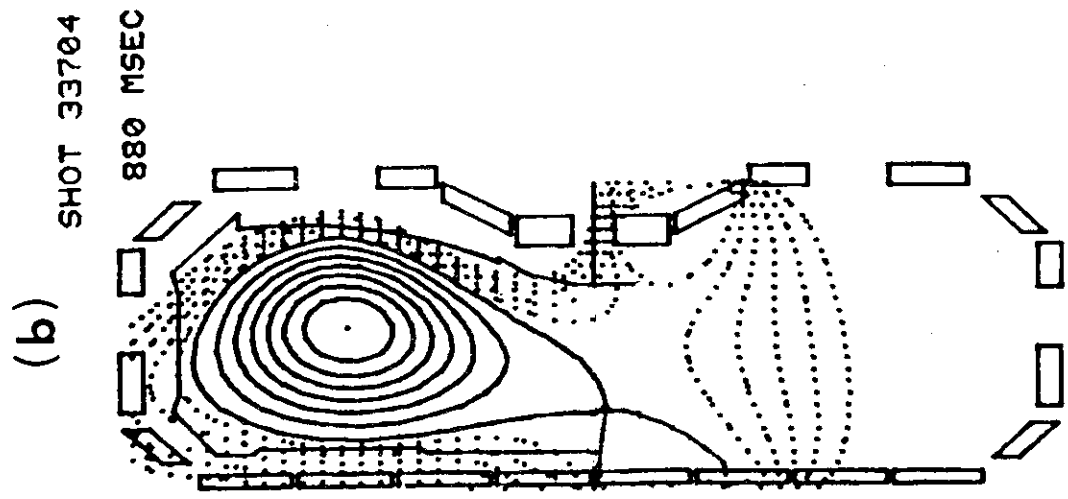

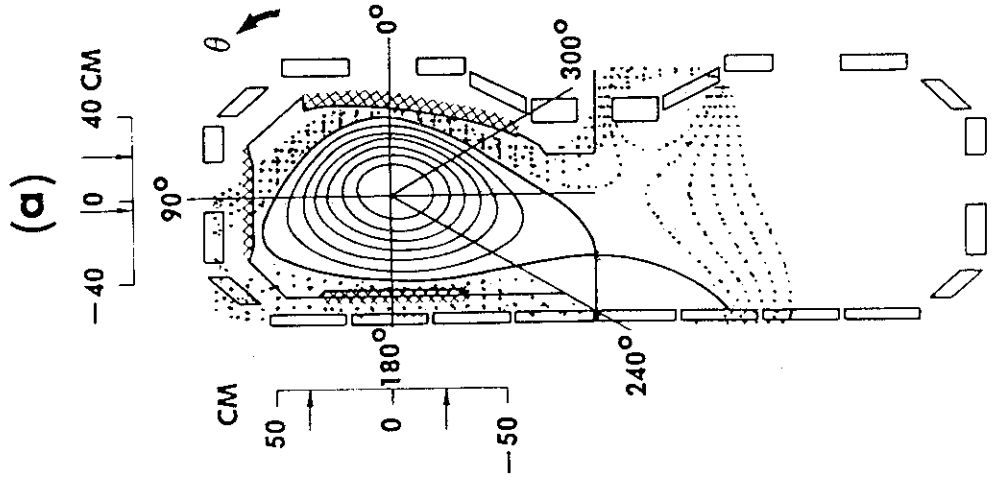

Fig. 1

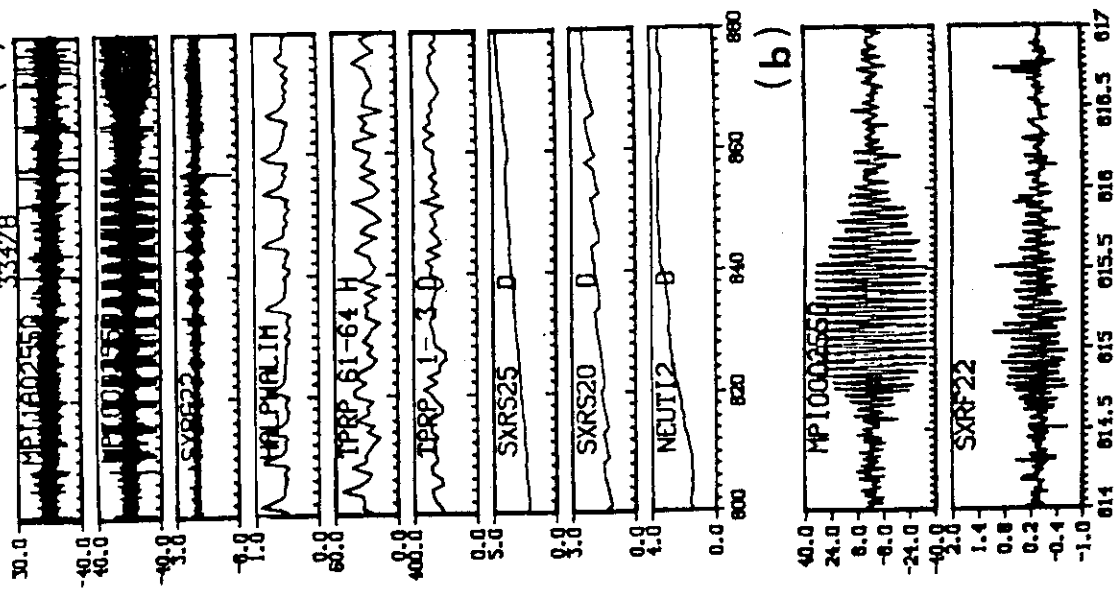

Fig. 3

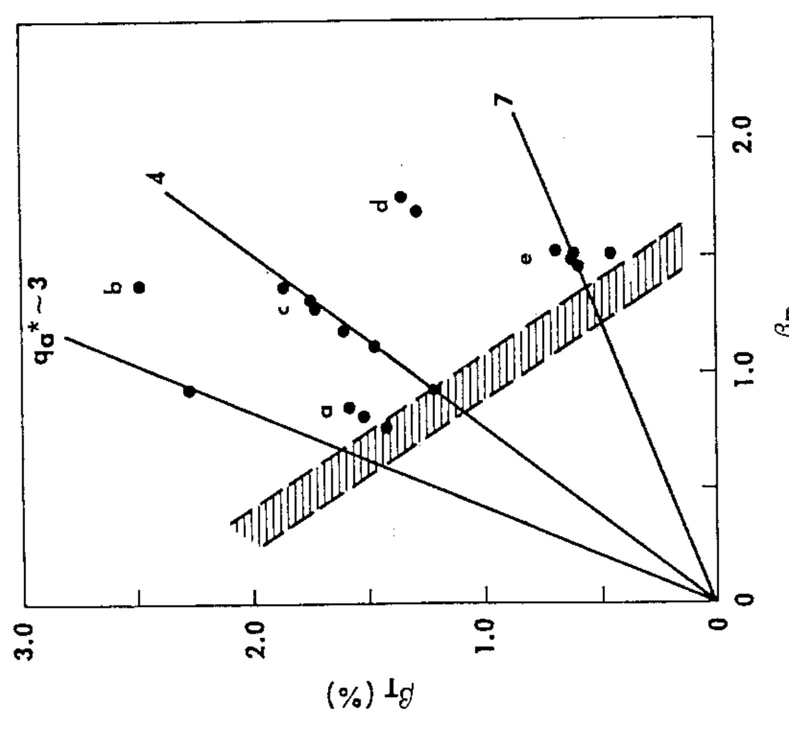

Fig. 2

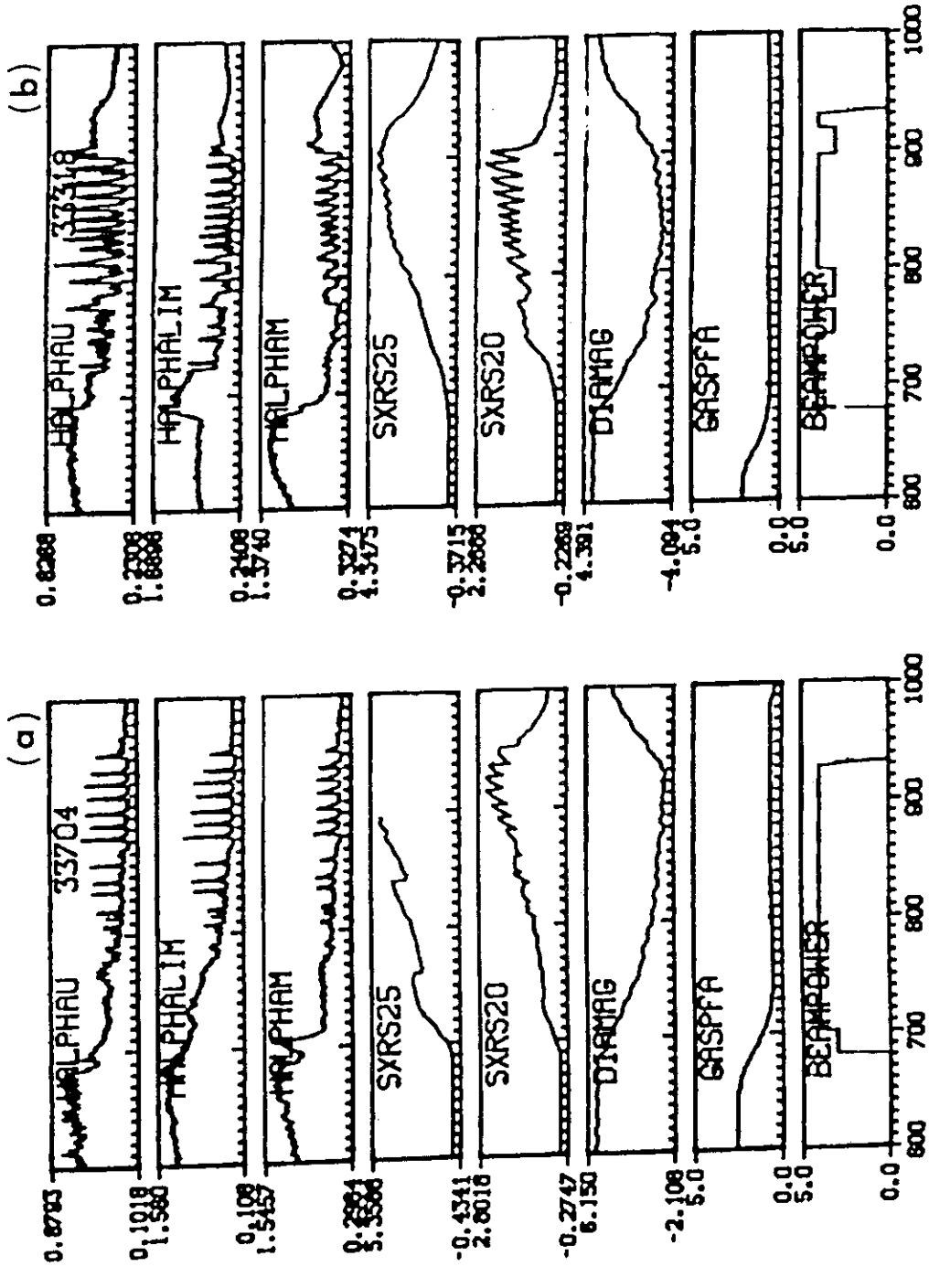
(a)
33704
HALPHAU
HALPHALIM
HALPHAM
SXRS25
SXRS20
DIAMAG
GASPFA
BEAMPOWER
800
700
800
800
1000
(b)
33318
HALPHAU
HALPHALIM
HALPHAM
SXRS25
SXRS20
DIAMAG
GASPFA
BEAMPOWER
800
700
800
800
1000

Fig. 4

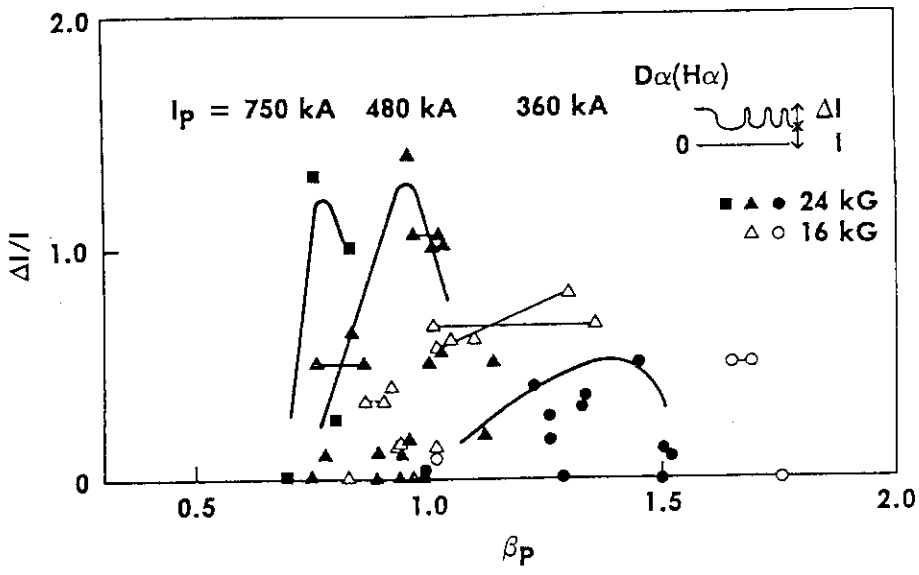
2.0
1.0
0
ΔI/I
Dα(Hα)
ΔI
0
I
Ip = 750 kA 480 kA 360 kA
■ ▲ ● 24 kG
△ ○ 16 kG
0.5
1.0
1.5
2.0
βp

Fig. 5

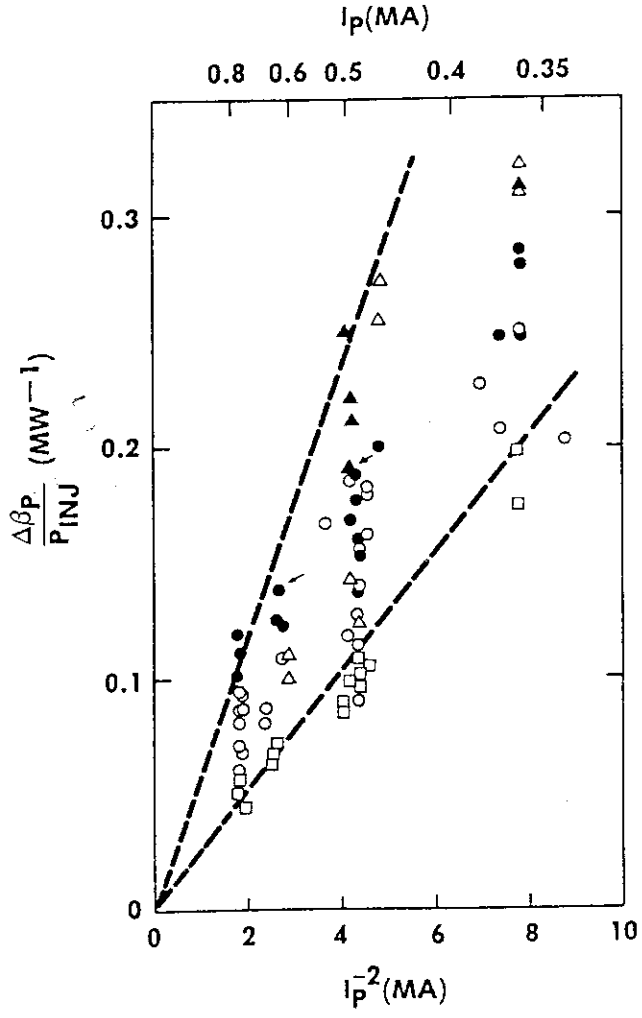
Ip(MA)
0.8 0.6 0.5 0.4 0.35
0.3
0.2
0.1
0
Δβp/PINJ (MW⁻¹)
0 2 4 6 8 10
Ip⁻²(MA)

Fig. 6

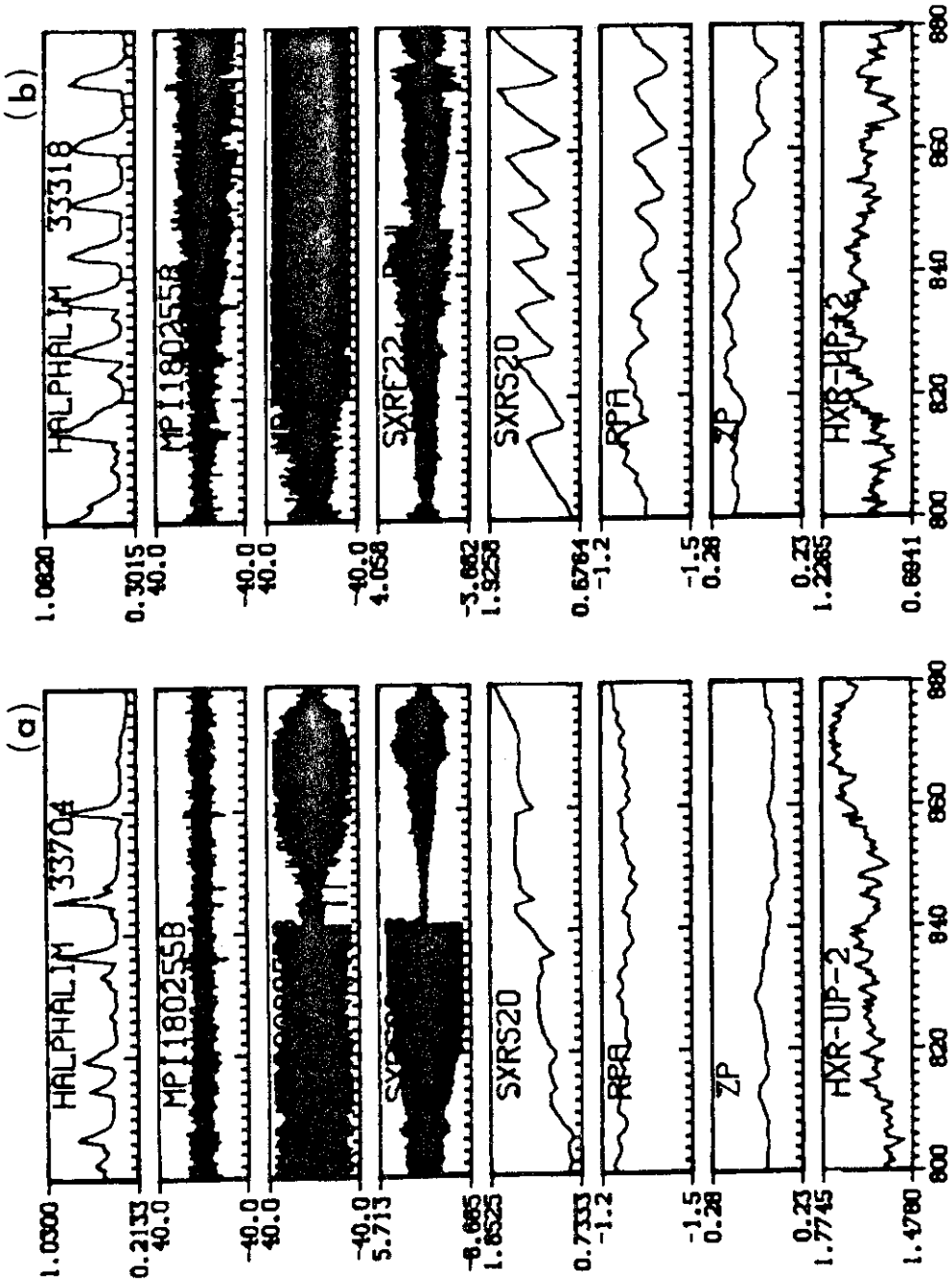
(a)
HALPHALIM 33704
MPI1802558
SXRS20
RPA
ZP
HXR-UP-2
(b)
HALPHALIM 33318
MPI1802558
SXRF22
SXRS20
RPA
ZP
HXR-UP-2

Fig. 7

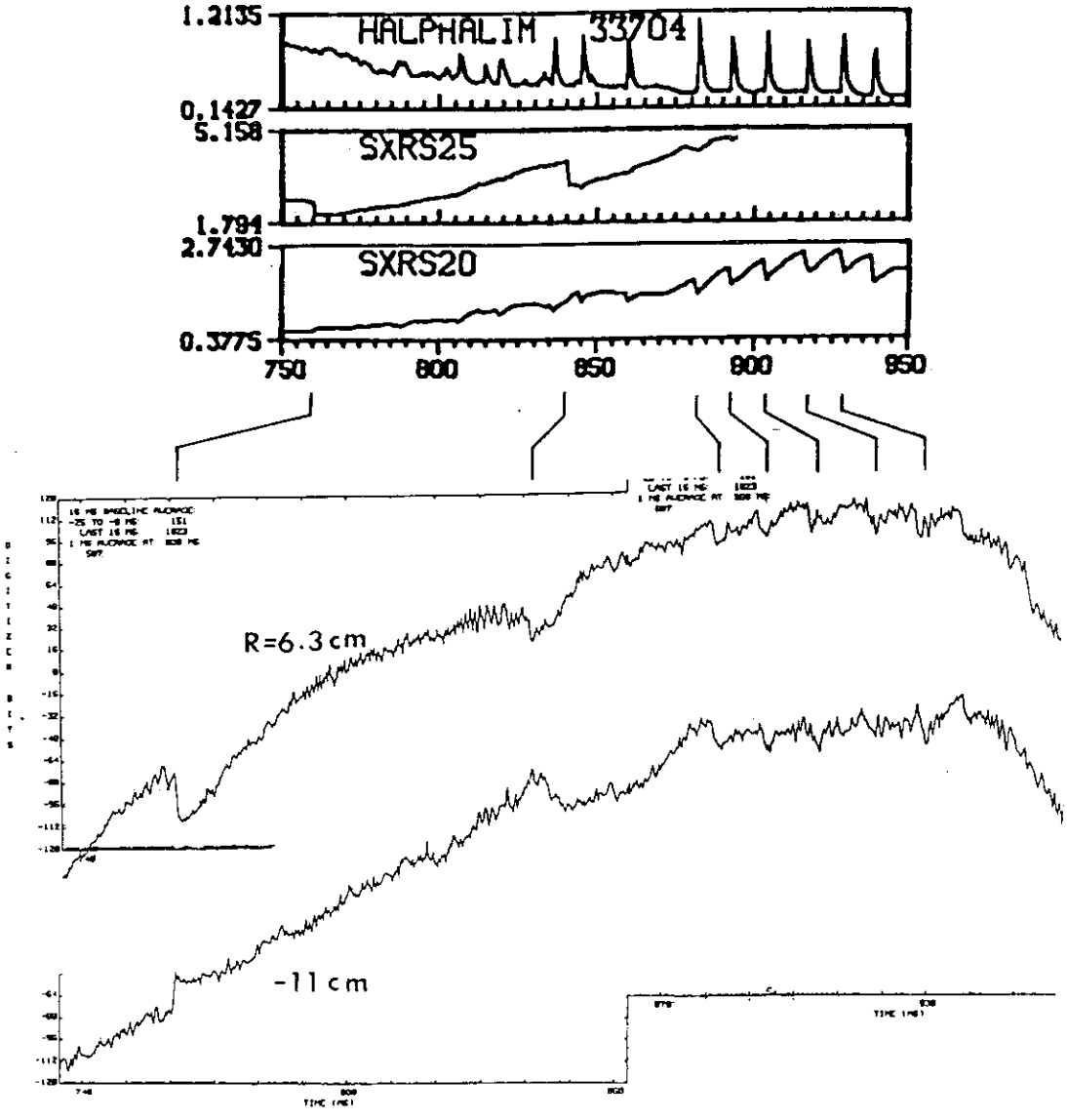
1.2135
HALPHALIM 33704
0.1427
5.158
SXRS25
1.794
2.7430
SXRS20
0.3775
750
800
850
900
950
R=6.3 cm
-11 cm

Fig. 8

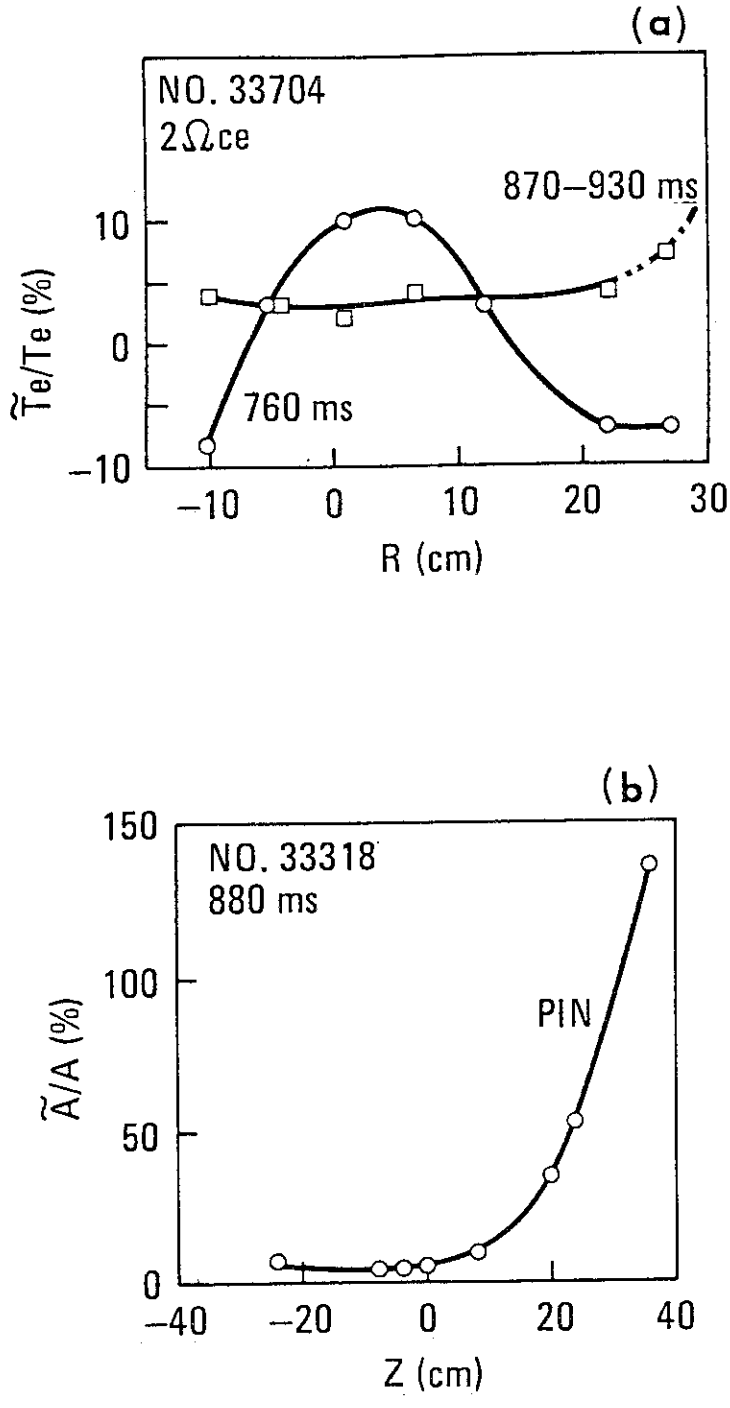
(a)
NO. 33704
2Ωce
870–930 ms
760 ms
10
0
−10
−10
0
10
20
30
R (cm)
Te/Te (%)
(b)
NO. 33318
880 ms
PIN
150
100
50
0
−40
−20
0
20
40
Z (cm)
Ã/A (%)

Fig. 9

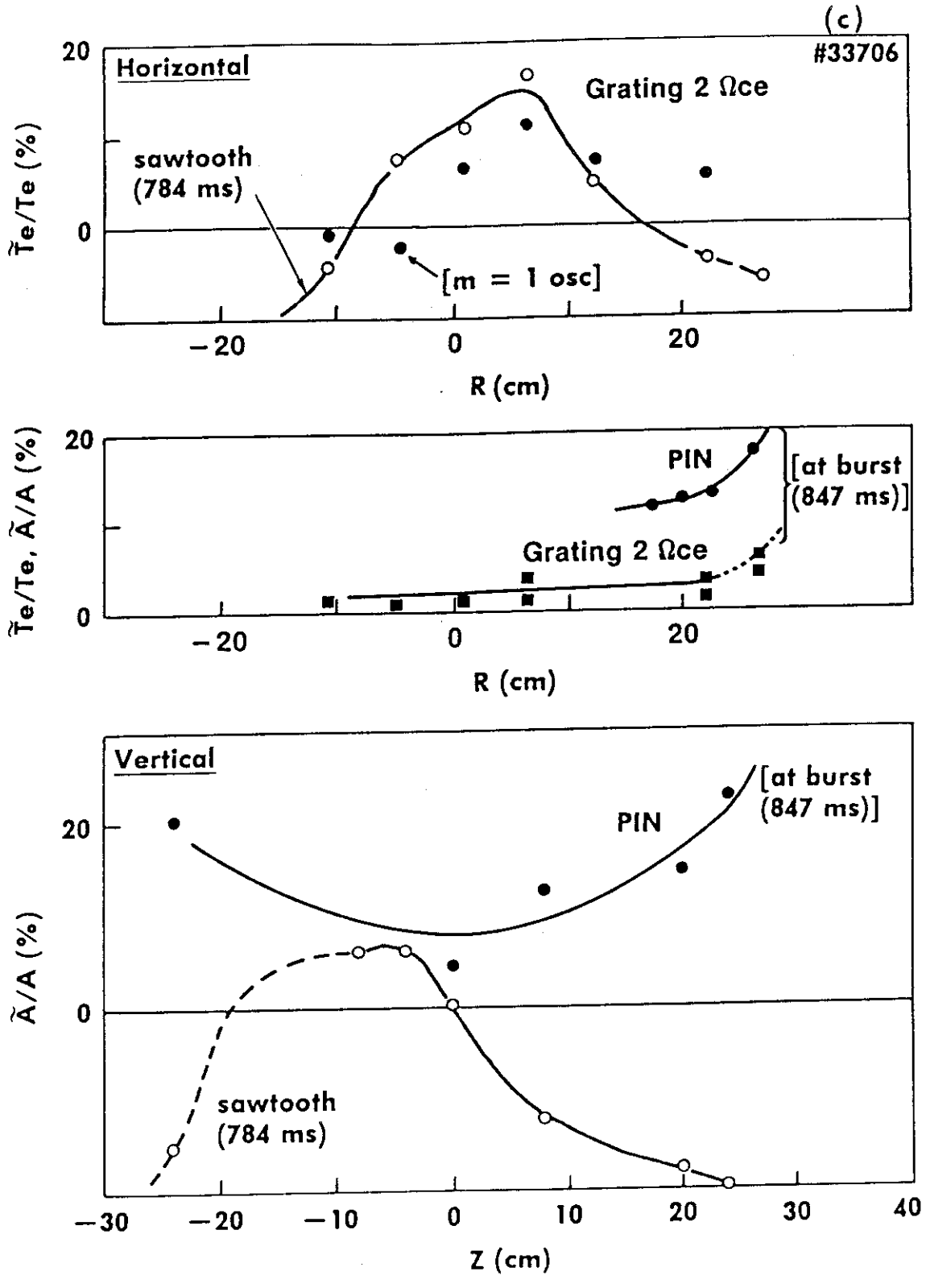
(c)
#33706
Horizontal
Grating 2 Ωce
sawtooth
(784 ms)
[m = 1 osc]
20
0
−20
0
20
R (cm)
T̃e/Te (%)
PIN
[at burst
(847 ms)]
Grating 2 Ωce
T̃e/Te, Ã/A (%)
Vertical
Ã/A (%)
Z (cm)
−30
−10
10
30
40

Fig. 9

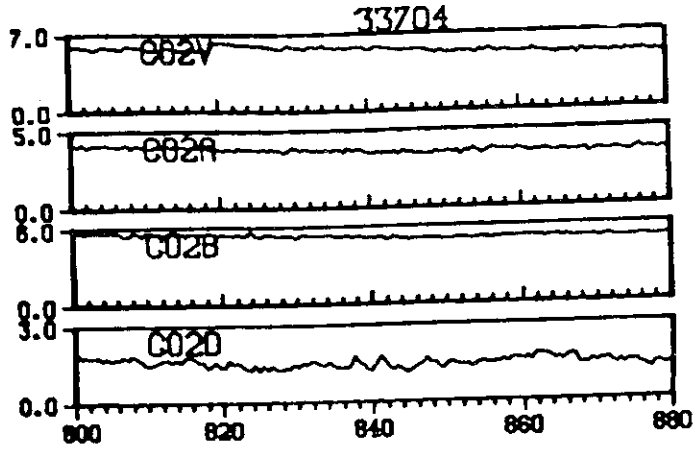
33704
7.0
C02V
0.0
5.0
C02A
0.0
6.0
C02B
0.0
3.0
C02D
0.0
800
820
840
860
880

Fig. 10

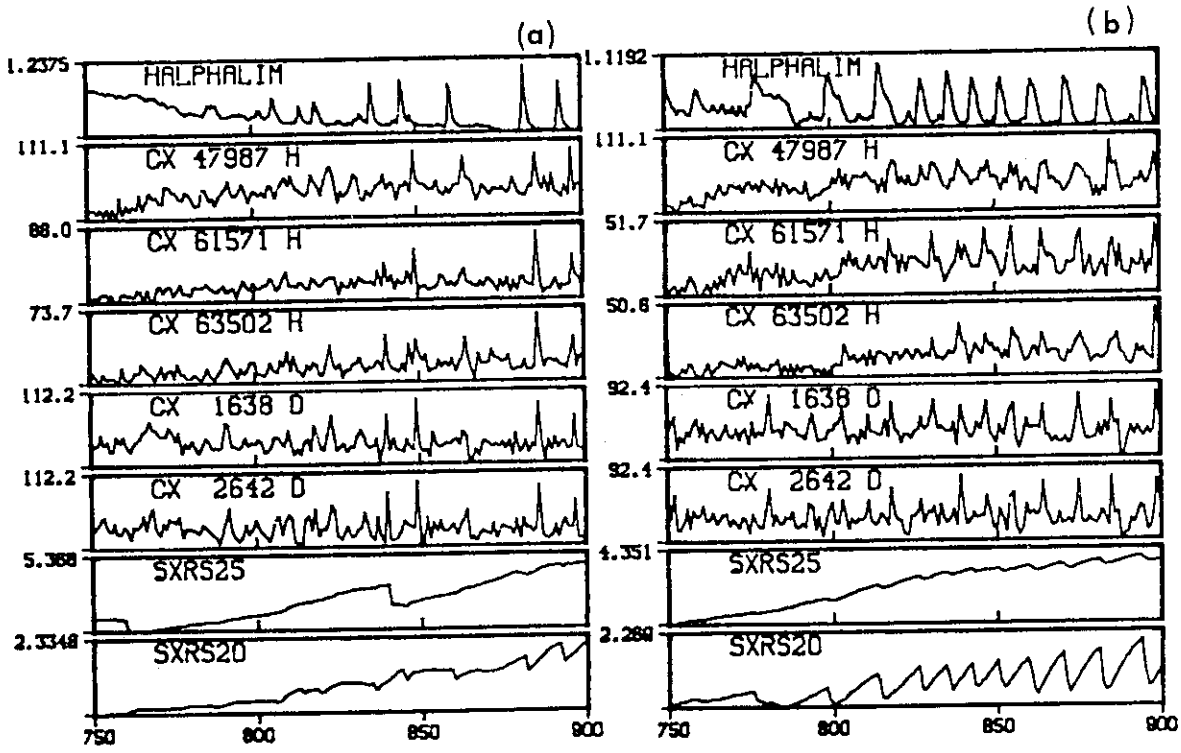
(a)
(b)
1.2375
HALPHALIM
111.1
CX 47987 H
88.0
CX 61571 H
73.7
CX 63502 H
112.2
CX 1638 D
112.2
CX 2642 D
5.368
SXR525
2.3348
SXR520
750
800
850
900
1.1192
HALPHALIM
111.1
CX 47987 H
51.7
CX 61571 H
50.6
CX 63502 H
92.4
CX 1638 D
92.4
CX 2642 D
4.351
SXR525
2.280
SXR520
750
800
850
900

Fig. 11

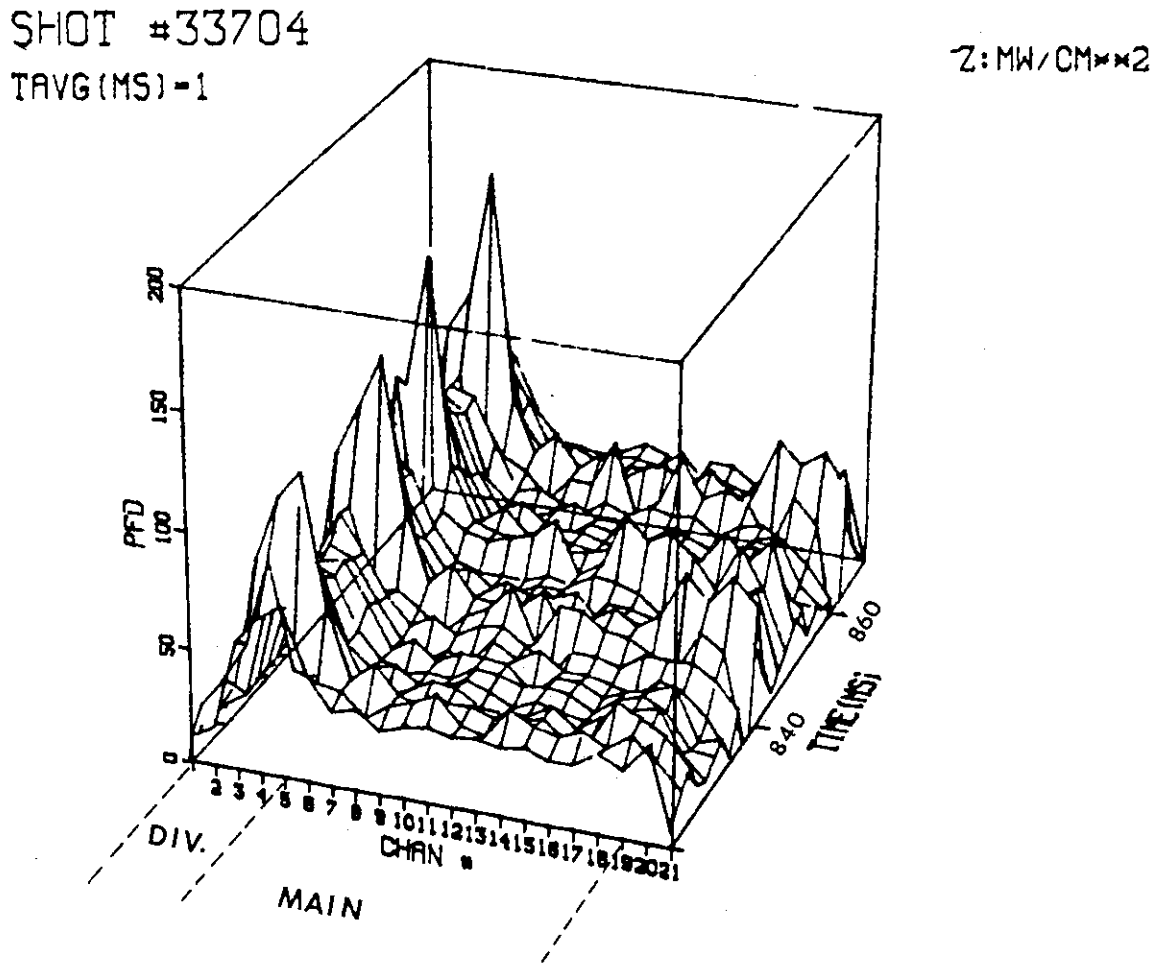
SHOT #33704
TAVG(MS)=1
Z:MW/CM**2
200
150
100
50
0
PFD
DIV.
MAIN
CHAN #
1 2 3 4 5 6 7 8 9 10 11 12 13 14 15 16 17 18 19 20 21
840
860
TIME(MS)

Fig. 12

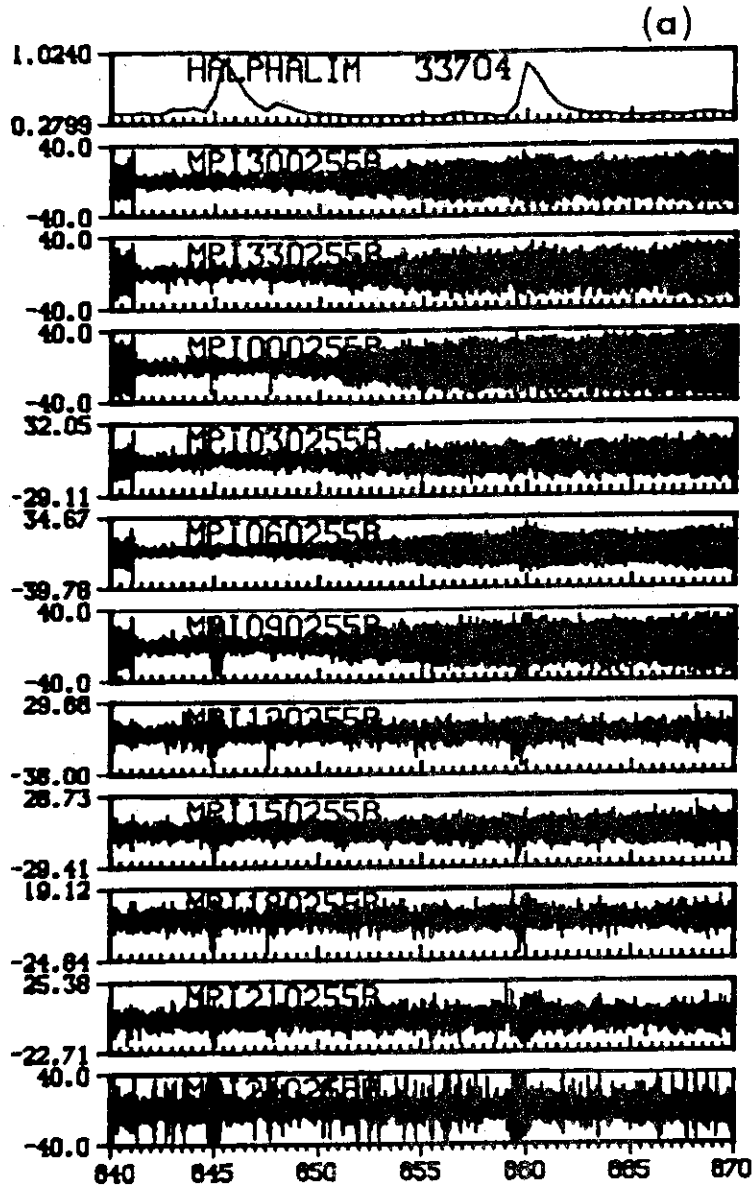
(a)
1.0240
HALPHALIM 33704
0.2799
40.0
-40.0
40.0
-40.0
40.0
-40.0
32.05
-29.11
34.67
-39.78
40.0
-40.0
29.66
-38.00
28.73
-29.41
19.12
-24.64
25.38
-22.71
40.0
-40.0
640
645
650
655
660
665
670

Fig. 13

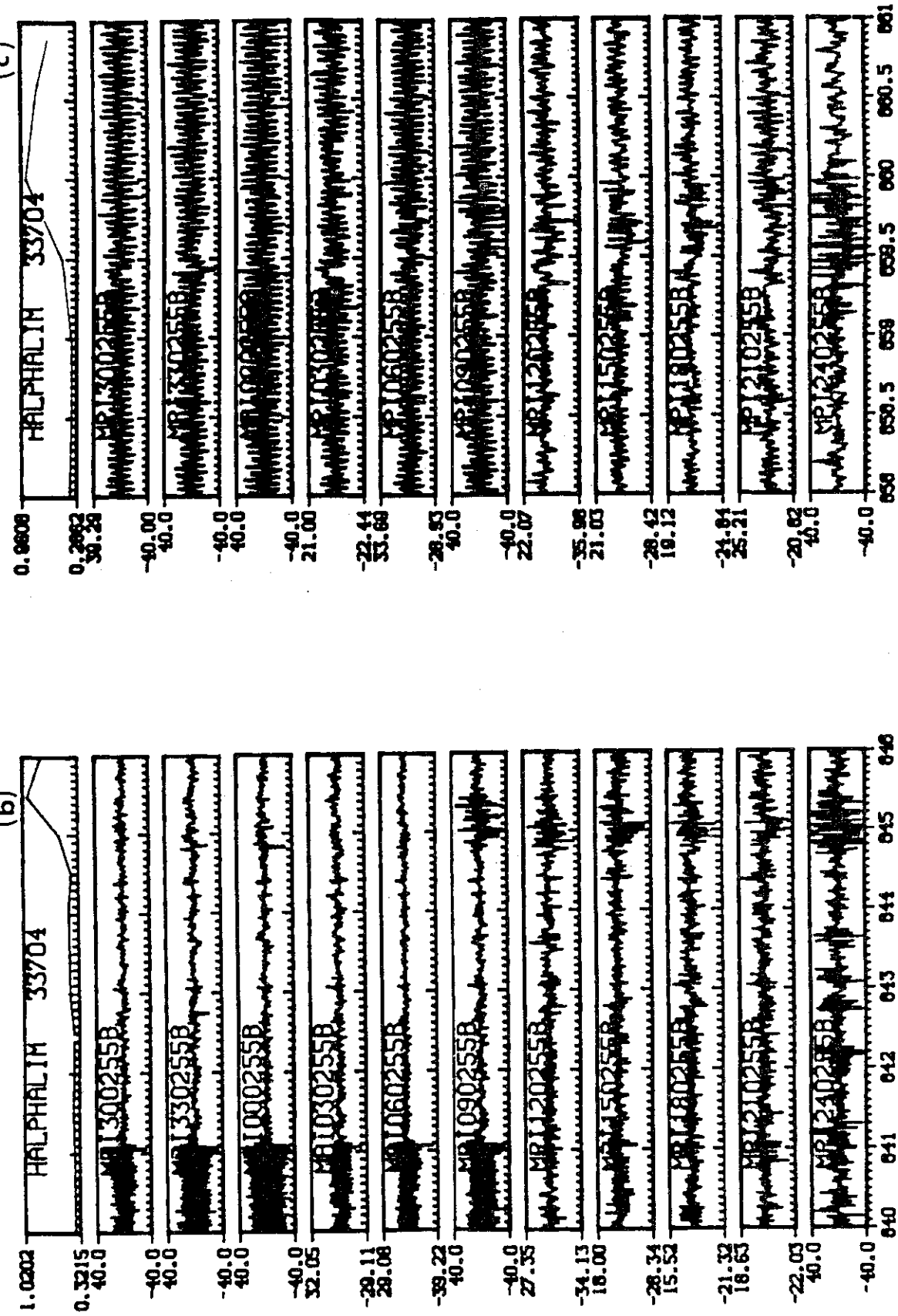

Fig. 13

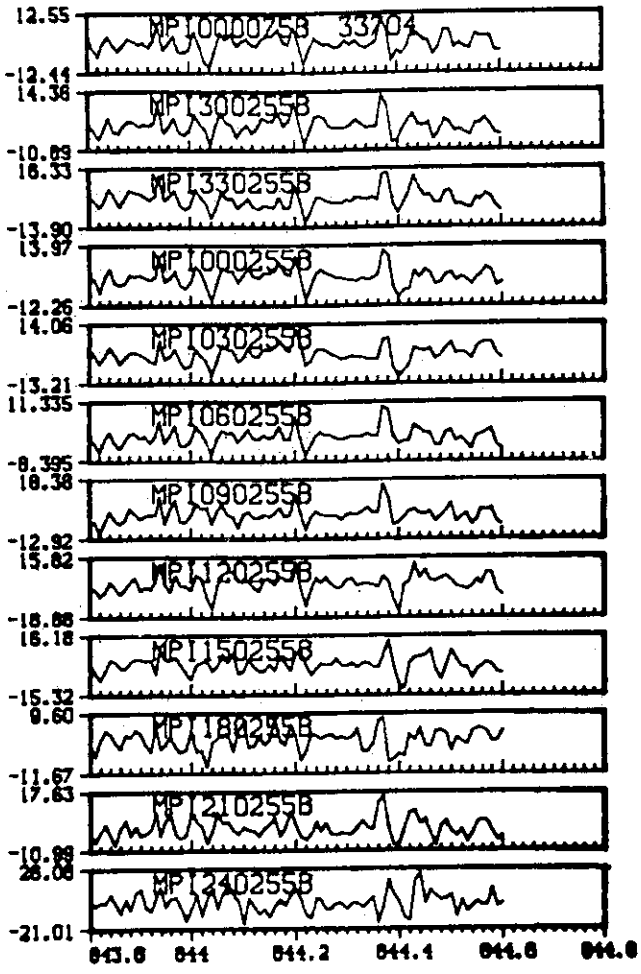
12.55
-12.44
14.36
-10.69
16.33
-13.90
13.97
-12.26
14.06
-13.21
11.335
-8.395
10.38
-12.92
15.82
-16.88
16.18
-15.32
9.60
-11.67
17.83
-10.88
-21.01
843.6
844
844.2
844.4
844.6
844.8

Fig. 14

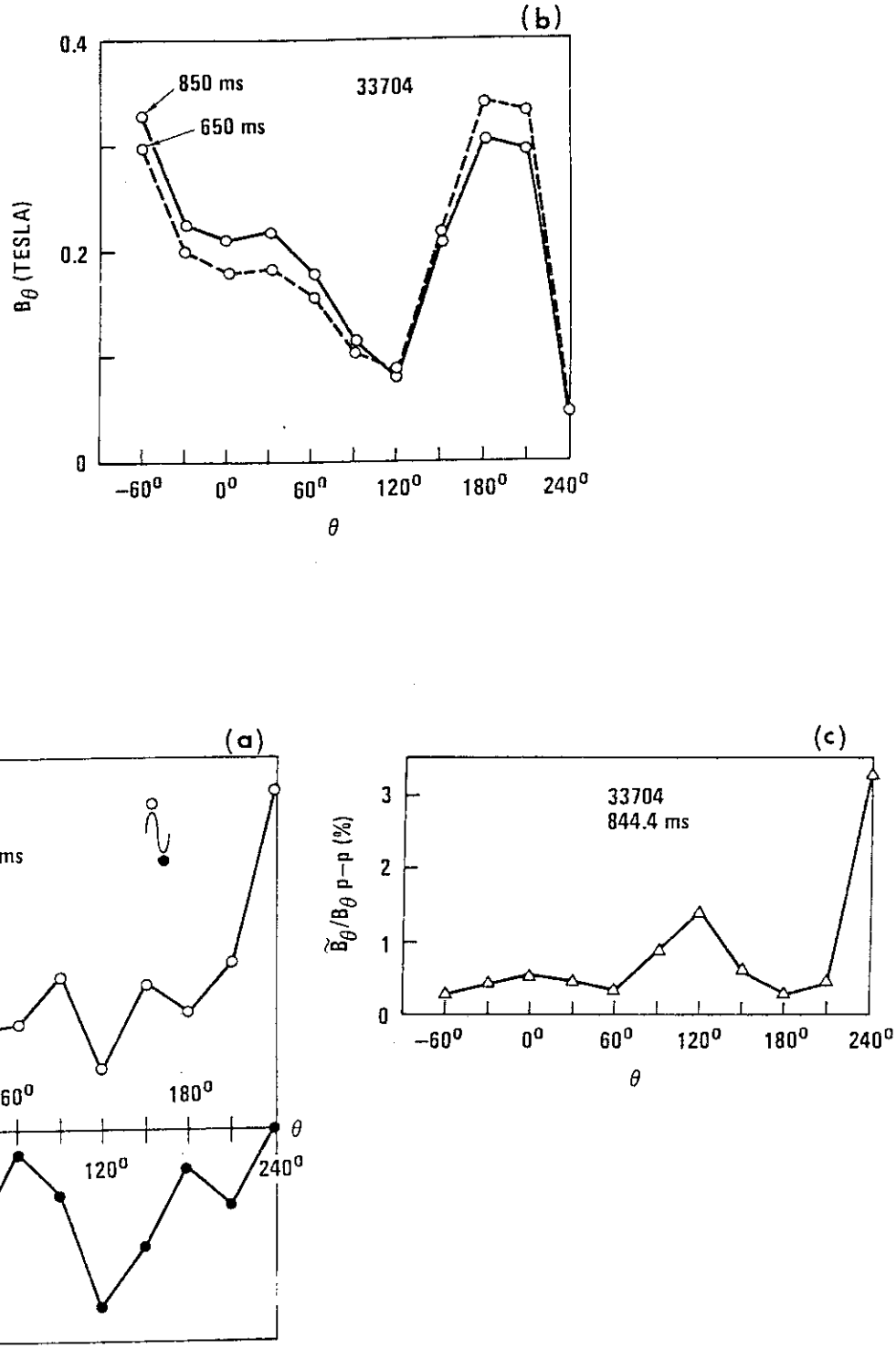
(b)
0.4
0.2
0
850 ms
650 ms
33704
B_θ (TESLA)
−60°
0°
60°
120°
180°
240°
θ
(a)
33704
844.4 ms
20
0
−20
60°
180°
θ
−60°
0°
120°
240°
$\tilde{B}_\theta$ (T/S)
(c)
33704
844.4 ms
3
2
1
0
$\tilde{B}_\theta/B_\theta$ p−p (%)
−60°
0°
60°
120°
180°
240°
θ

Fig. 15

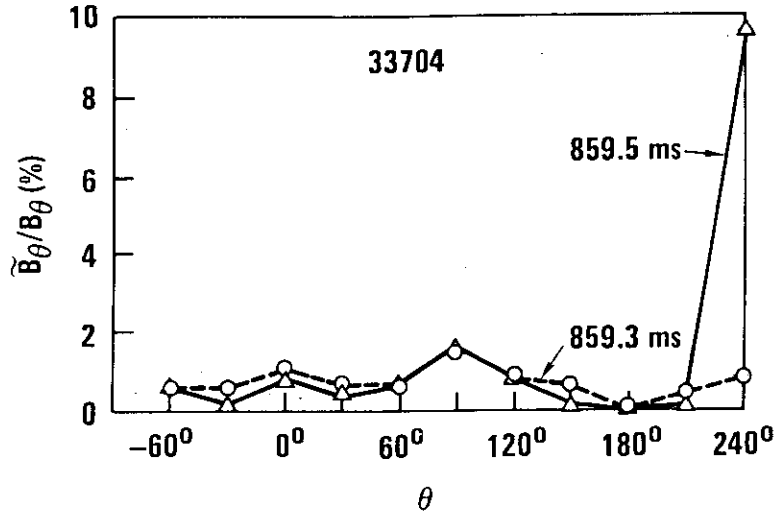
33704
859.5 ms
859.3 ms
$\tilde{B}_\theta/B_\theta$ (%)
10
8
6
4
2
0
-60^0
0^0
60^0
120^0
180^0
240^0
θ

Fig. 16